

 Open access • Posted Content • DOI:10.1101/2021.03.15.435473

MCMICRO: A scalable, modular image-processing pipeline for multiplexed tissue imaging — [Source link](#)

[Denis Schapiro](#), [Denis Schapiro](#), [Artem Sokolov](#), [Clarence Yapp](#) ...+22 more authors

Institutions: [Broad Institute](#), [Harvard University](#), [Vanderbilt University Medical Center](#), [Vanderbilt University](#) ...+4 more institutions

Published on: 16 Mar 2021 - [bioRxiv](#) (Cold Spring Harbor Laboratory)

Topics: [Image processing](#)

Related papers:

- [Highly multiplexed immunofluorescence imaging of human tissues and tumors using t-CyCIF and conventional optical microscopes](#)
- [Deep Profiling of Mouse Splenic Architecture with CODEX Multiplexed Imaging.](#)
- [Multiplexed ion beam imaging of human breast tumors](#)
- [Highly multiplexed imaging of tumor tissues with subcellular resolution by mass cytometry](#)
- [Immuno-SABER enables highly multiplexed and amplified protein imaging in tissues.](#)

Share this paper:    

View more about this paper here: <https://typeset.io/papers/mcmicro-a-scalable-modular-image-processing-pipeline-for-400koiq9f8>

1 **MCMICRO: A scalable, modular image-processing pipeline for multiplexed tissue imaging**

2

3 Denis Schapiro^{1,2,3}, Artem Sokolov^{1,2}, Clarence Yapp^{1,2,4}, Jeremy L. Muhlich^{1,2}, Joshua Hess⁵, Jia-
4 Ren Lin^{1,2}, Yu-An Chen^{1,2}, Maulik K. Nariya^{1,2}, Gregory J. Baker^{1,2}, Juha Ruukonen^{1,2}, Zoltan
5 Maliga^{1,2}, Connor A. Jacobson^{1,2}, Samouil L. Farhi³, Domenic Abbondanza³, Eliot T. McKinley^{6,7},
6 Courtney Betts⁸, Aviv Regev^{3,9,10}, Robert J. Coffey¹¹, Lisa M. Coussens^{8,12}, Sandro Santagata^{1,2,13}
7 and Peter K. Sorger^{1,2,14}

8

9 The Human Tumor Atlas Network

10 ¹Ludwig Center for Cancer Research at Harvard, Harvard Medical School, Boston, MA

11 ²Laboratory of Systems Pharmacology, Harvard Medical School, Boston, MA

12 ³Klarman Cell Observatory, Broad Institute of MIT and Harvard, Cambridge, MA

13 ⁴Image and Data Analysis Core, Harvard Medical School, Boston, MA

14 ⁵Vaccine and Immunotherapy Center, Massachusetts General Hospital, Harvard Medical School,
15 Boston, MA

16 ⁶Epithelial Biology Center, Vanderbilt University Medical Center, Nashville, TN

17 ⁷Department of Cell and Developmental Biology, Vanderbilt University School of Medicine,
18 Nashville, TN

19 ⁸Department of Cell, Developmental & Cancer Biology, Oregon Health & Science University,
20 Portland, OR

21 ⁹Department of Biology, Howard Hughes Medical Institute, Massachusetts Institute of Technology,
22 Cambridge, MA, USA

23 ¹⁰Present address: Genentech, South San Francisco, CA, USA

24 ¹¹Division of Gastroenterology, Hepatology, and Nutrition, Department of Medicine, Vanderbilt
25 University Medical Center, Nashville, TN

26 ¹²Knight Cancer Institute, Oregon Health & Science University, Portland, OR

27 ¹³Department of Pathology, Brigham and Women's Hospital, Harvard Medical School, Boston, MA

28 ¹⁴Department of Systems Biology, Harvard Medical School, Boston, MA

29

30 Corresponding author:

31 Peter K. Sorger, Harvard Medical School, 200 Longwood Avenue, Warren Alpert Building, Room
32 440, Boston, MA 02115; Telephone: 617-432-6901; email: peter_sorger@hms.harvard.edu;

33 sorger_admin@hms.harvard.edu

34

35 **ABSTRACT**

36 Highly multiplexed tissue imaging makes molecular analysis of single cells possible in a
37 preserved spatial context. However, reproducible analysis of the underlying data poses a substantial
38 computational challenge. Here we describe a modular and open-source computational pipeline
39 (MCMICRO) for performing the sequential steps needed to transform large, multi-channel whole
40 slide images into single-cell data. We demonstrate use of MCMICRO on images of different tissues
41 and tumors acquired using multiple imaging platforms, thereby providing a solid foundation for the
42 continued development of tissue imaging software.

43

44 **MAIN**

45 The recent introduction of highly multiplexed tissue imaging makes it possible to measure the
46 levels and localization of 20-100 antigens at subcellular resolution in a preserved 3D environment
47 (see **Table S1** for references). In a research setting, multiplexed imaging provides new insight into
48 molecular properties of tissues and their spatial organization and, in a clinical setting, it promises to
49 augment traditional histopathological diagnosis of disease with the molecular information needed to
50 guide use of targeted and immuno-therapies¹⁻⁴. Inadequate tools for image processing remain a
51 substantial barrier to the routine use of multiplexed tissue imaging, particularly in the case of whole-
52 slide imaging (WSI), in which specimens as large as 5 cm² are imaged in their entirety. Diagnostic
53 histopathology is based on WSI, and the FDA mandates it for medical applications^{5,6}. We have also
54 found that multiplexed WSI is essential for accurately quantifying the mesoscale structures that
55 organize tissues⁷. Whole-slide images can contain one terabyte of data, 10⁵ to 10⁶ cells, and involve
56 resolvable structures with spatial scales from 100 nm to over 1 cm. This represents a substantial
57 challenge for computational image analysis.

58 A goal common to almost all multiplexed tissue analyses is identifying cell locations,
59 phenotypes and states based on the levels and patterns of expression of protein markers. These are
60 usually detected using antibodies, often in conjunction with stains such as hematoxylin and eosin
61 (H&E). Image-based single-cell analysis is a natural complement to spatial and single-cell
62 transcriptomics⁸⁻¹⁰ but faces four computational challenges: (i) image segmentation, the process of
63 subdividing images into areas comprising single cells, is difficult when normal tissue structures are
64 disrupted, cells are densely crowded, and nuclei have irregular morphologies – as in cancer; (ii) the
65 fundamental units of tissue organization are highly variable, and the essential data types are not well
66 defined; (iii) WSI generates very large files that must be available for human inspection (a 50-plex 4
67 cm² image collected at 0.3μm lateral resolution comprises over 400 GB of data); (iv) image
68 processing algorithms are simultaneously being developed by many research groups in parallel,

69 using different programming languages (some proprietary, such as MATLAB) without consideration
70 of interoperability. Analogous challenges in genomics have been addressed by developing
71 computational pipelines that streamline multi-step data analyses and can also be scaled up to cloud
72 compute environments (e.g., Cumulus for scRNAseq)¹¹. The use of pipelines involving software
73 containers (e.g., Docker¹²) and workflow languages¹³ makes it possible for multiple research groups
74 to contribute to and iteratively improve complex computational tasks. In the case of tissue atlases,
75 such as the Human Tumor Atlas Network (HTAN)¹⁴, multiple laboratories are faced with a common
76 set of data analysis challenges, a further motivation for a standardized computational framework.

77 In this paper we describe MCMICRO (Multiple Choice MICROscopy), a scalable, modular,
78 and open source image processing pipeline implemented in the Nextflow language¹⁵ that leverages
79 Docker/Singularity containers^{12,16}. We show that MCMICRO can process multiplexed data acquired
80 using at least six different imaging technologies (**Table S1**) and has attributes not found in existing
81 workflows (**Table S2**). These include the ability to select among competing algorithms at key steps
82 in the analysis and interactive training of machine learning models (this is particularly important for
83 image segmentation). In common with other bioinformatics pipelines, MCMICRO is designed to
84 complement rather than replace conventional desktop and server-deployed tools. A wide variety of
85 algorithms can be incorporated into the MCMICRO pipeline using containers, and the results can be
86 visualized using multiple software environments, including napari, QuPath, OMERO and histoCAT
87 (see **Table S2** for details and references).

88 To create MCMICRO, we re-implemented as open-source software several algorithms
89 previously available in the proprietary language MATLAB (MCQuant for quantifying marker
90 intensities and computing morphology metrics¹⁷, and S3segmenter for watershed segmentation¹⁸,
91 spot detection, and local thresholding). We also containerized several open-source algorithms
92 (BaSiC¹⁹ and Ilastik²⁰), and incorporated three algorithms and associated deep learning models
93 developed in our laboratories (UMAP/UnMicst, Coreograph and ASHLAR) (**Fig. 1A**; module names
94 in red). All algorithms were tuned to manage very large files (~ 500GB/image) and containerized to
95 abstract away language-specific dependencies (**Methods**). Source code, a user guide and other
96 training materials are available via GitHub (<https://github.com/labsyspharm/mcmicro>).

97 To facilitate benchmarking, development of new algorithms and model training, we also
98 generated a set of freely available reference images, the Exemplar Microscopy Images of Tissues and
99 Tumors (EMIT). EMIT comprises multiplexed CyCIF images of a tissue microarray (TMA) with
100 120 1.5 mm cores from 34 types of cancer, non-neoplastic diseases, and matched normal tissue
101 (**Figure S1**, <https://synapse.org/EMIT>). EMIT images were processed using MCMICRO (using the
102 Coreograph module) and all steps are documented on Synapse (<https://synapse.org/EMIT>).

103 Clustering of normal tissues and cancers by type (with some variance, because specimens came from
104 different individuals) demonstrates that a wide range of specimens can be processed by MCMICRO
105 to generate meaningful single cell data (**Figure S2**).

106 Processing multiplexed WSI data starts with acquisition of individual image tiles in a
107 BioFormats-compatible format (level 1 data; **Fig. 1A**)²¹; each tile is typically a megapixel
108 multichannel image, and as many as 10^3 tiles are required to cover a large tissue specimen at
109 subcellular resolution. Tiles are corrected for uneven illumination, stitched together, and registered
110 across channels to generate the first broadly useful type of data: a fully assembled, multichannel
111 *mosaic image* in OME-TIFF format (a class of level 2 data) (**Fig. 1B**). In a large mosaic whole-slide
112 image, length scales vary 10^5 -fold from the smallest resolvable feature to the largest dimension.
113 Images are subjected to quality control, followed by segmentation. A segmentation mask (level 3
114 data), the next object computed by MCMICRO, is available for human inspection in conjunction
115 with underlying images to determine the quality of different segmentation approaches (**Fig. 1C**).

116 Following segmentation, the staining intensity in each channel is computed on a per-cell
117 basis to generate a *Spatial Feature Table* (level 4 data), which is analogous to a count table in
118 scRNAseq. In its simplest form, this table consists of the positions of cells and their integrated
119 staining intensities in each imaging channel (morphological data, such as size, eccentricity etc. are
120 additional table elements; **Fig. 1D**). The Spatial Feature Table can be visualized using tools designed
121 for high dimensional data such as tSNE or UMAP, processed to identify cell types, and used for
122 neighborhood or other types of analysis (**Fig. 1D**). It is also possible to skip segmentation altogether
123 and perform analysis directly on images; pixel-level deep learning has already shown promise in
124 clinical settings^{22,23}, and many algorithms have been generalized for use with multiplexed data.
125 Regardless of how data flows through MCMICRO, provenance is maintained by recording the
126 identities, version numbers and parameter settings for each module, enabling full reproducibility
127 (**Fig. S3**).

128 MCMICRO includes a newly developed tool for processing TMAs, which are widely used in
129 research, because they enable parallel analysis of many specimens. In a TMA, a single slide carries
130 dozens to hundreds of 0.3 to 2 mm diameter “cores”. The *Coreograph* module in MCMICRO is
131 based on the U-Net deep learning architecture²⁴. It finds the locations of individual cores and extracts
132 each core as a separate, multi-channel image (**Fig. 1E**), allowing all cores to be processed in parallel
133 by downstream modules. The robustness of the underlying neural network makes it possible for the
134 module to accurately identify cores even in highly distorted TMAs.

135 Image processing requires user interaction and frequent visual review (see CellProfiler, for
136 example²⁵). To enable human-in-the-loop analysis, MCMICRO allows for training and parameter

137 adjustment to take place locally, using subsets of a large mosaic image. This iterative approach is
138 particularly important for segmentation, since most contemporary algorithms rely on supervised
139 machine learning. An absence of well-defined objective functions and ground truth data makes
140 automated scoring of algorithms difficult, and different combinations of algorithms and models may
141 be optimal for different tissues. MCMICRO therefore incorporates multiple segmentation algorithms
142 (e.g., U-Net²⁴ or ilastik²⁰), which can be executed in parallel and then compared (**Fig. 1C**).
143 Additional improvement in segmentation can be achieved with the help of the EMIT data repository
144 (<https://synapse.org/EMIT>), which includes a “classifier zoo” comprising a set of tissue-specific
145 random forest segmentation models for ilastik. These models aid generation of robust tissue-specific
146 segmentation masks and can also be subjected to further dataset-specific training.

147 To demonstrate the technology-agnostic capabilities of MCMICRO, we collected data from a
148 single FFPE tonsil specimen at four different institutions using four imaging technologies: CODEX
149 and CyCIF, which are immunofluorescence-based; mIHC, which uses multiplexed
150 immunohistochemistry; and H&E staining (**Fig. 2A**). We also analyzed mxIF and publicly available
151 Imaging Mass Cytometry (IMC) and MIBI data (**Table S2**). To show that MCMICRO does not have
152 specific hardware dependencies, data processing was performed using cloud compute nodes
153 provided either by Amazon Web Services (AWS) or the Google Cloud Platform and also using a
154 Linux-based institutional cluster running the SLURM workload manager. MCMICRO provides
155 detailed information on time, memory and CPU usage, making it straightforward to provision
156 necessary computational resources (**Fig. S4**).

157 Image tiles from a variety of microscopes were subjected to stitching, registration and
158 illumination correction using ASHLAR and BaSiC to generate mosaic level 2 image data that was
159 visually inspected on a local workstation using napari and in the cloud using OMERO (**Fig. 2A**).
160 Images were then segmented and staining intensities were computed on a per-cell basis using
161 MCQuant. Cell types were visualized in the tissue context for epithelial cells of the tonsil mucosa
162 (Keratin+/panCK+), cytotoxic T cells (CD8+) and B cells (CD20+) (**Fig. 2B**). Visual inspection of
163 stitched and registered CyCIF, CODEX and mIHC images and derived data revealed accurate image
164 stitching and registration, facilitating the creation of reasonable segmentation masks and the
165 generation of correctly formatted Spatial Feature Tables. The results of cell type calling were similar
166 (**Fig. 2C**), and when data from all three technologies were combined and visualized using tSNE,
167 cells were separated by marker expression not imaging technology (**Fig 2D**). These findings
168 demonstrate consistency in image acquisition and data processing.

169 A few algorithms in MCMICRO (e.g., Ashlar and BaSiC) are tissue and technology agnostic
170 and can be used on diverse types of data with little, if any, tuning or modification. The performance

171 of other algorithms (e.g., UnMicst and Ilastik) is dependent on the properties of their learned models,
172 which often work well for some tissues and not for others. MCMICRO facilitates identification of
173 effective algorithms and models by executing different segmentation approaches in parallel,
174 followed by comparison of the resulting masks. We expect continued innovation in the area of image
175 segmentation, as well as addition of algorithms for automated quality control of images and
176 identification of cell types based on marker intensities and cell morphologies. However, we do not
177 anticipate that users will need to manage an endless proliferation of novel methods: multiple research
178 consortia are actively working together on evaluation efforts (analogous to Dream Challenges²⁶)
179 aimed at creating best practices for highly-multiplexed image analysis. MCMICRO provides the
180 technical foundation for such evaluations and for widespread distribution of the results. MCMICRO
181 is also being used by the HTAN consortium to rigorously compare different image acquisition
182 technologies.

183 In conclusion, the MCMICRO pipeline described here provides a foundation for community-
184 wide development of FAIR (findable, accessible, interoperable and reusable)²⁷ workflows for
185 analysis of large tissue images currently being generated by multiple international consortia and
186 many individual laboratories. MCMICRO works with any acquisition technology that generates Bio-
187 Formats/OME-compatible images, including the six technologies described above. The pipeline is
188 based on widely accepted software standards and interoperates with any programming language
189 through the use of software containers, making it easy to add new modules. The result is a user-
190 friendly end-to-end pipeline that executes computation-intensive processes in the cloud, while
191 enabling parameter optimization, training and quality control to be performed locally and
192 interactively.

193

194 **METHODS**

195 Tissue samples

196 A de-identified tonsil specimen from a 4-year old Caucasian female was procured from the
197 Cooperative Human Tissue Network (CHTN), Western Division, as part of the Human Tumor Atlas
198 (HTAN) SARDANA trans-network project (TNP). Regulatory documents including Institutional
199 Review Board (IRB) protocols, data use agreements and tissue use agreements were in place to
200 ensure regulatory compliance. Standard protocols for tissue procurement and fixation were followed;
201 a detailed protocol can be found at the link provided in Table 1. Sections were cut from a common
202 formalin-fixed paraffin embedded (FFPE) block at a thickness of 5 μm and mounted onto Superfrost
203 Plus glass microscope slides (Fisher Scientific, 12-550-15) for CyCIF and mIHC or mounted on
204 poly-L-Lysine (PLL) coated coverslips (Electron Microscopy Sciences, 72204-01; slides and FFPE
205 sections prepared following instructions in the Akoya Biosciences CODEX User Manual Rev B.0,
206 Chapter 3. Coverslip Preparation and Tissue Processing) for CODEX. A set of FFPE tissue sections
207 was received by participating HTAN Centers, as indicated in **Table 1**, allowing Centers to generate a
208 comparable spatial cell census using each Center's imaging method of choice. CHTN performed
209 hematoxylin and eosin (H&E) staining on the first section which was subsequently imaged at
210 Harvard Medical School (HMS).

211 For the EMIT dataset, human tissue specimens (from 42 patients) were used to construct a
212 multi-tissue microarray (HTMA427) under an excess (discarded) tissue protocol approved by the
213 IRB at Brigham and Women's Hospital (BWH IRB 2018P001627). Two 1.5 mm diameter cores
214 were acquired from each of 60 tissue regions with the goal of acquiring one or two examples of as
215 many tumors as possible (with matched normal tissue from the same resection when that was
216 feasible), as a well several non-neoplastic medical diseases involving acute inflammation (e.g.
217 diverticulitis and appendicitis), and secondary lymphoid tissues such as tonsil, spleen and lymph
218 nodes. Overall, the TMA contained 120 cores plus 3 additional "marker cores," which are cores
219 added to the TMA in a manner that makes it possible to orient the TMA in images.

220

221 **Table 1. Sample information.**

Section Number	Section Thickness (μm)	Center	Assay
WD-75684-01	5	Cooperative Human Tissue Network	H&E
WD-75684-02	5	Harvard Medical School	CyCIF
WD-75684-05	5	Broad Institute	CODEX

WD-75684-08	5	Harvard Medical School	CyCIF
WD-75684-12	5	Oregon Health & Science University	mIHC

222

223 CyCIF staining and imaging

224 The CyCIF method involves iterative cycles of antibody incubation, imaging and fluorophore
 225 inactivation as described previously⁷. A detailed protocol can be found on protocols.io as shown in
 226 **Table 2**. CyCIF images are 36-plex whole-slide images collected using a 20x magnification, 0.75
 227 NA objective with 2 x 2 pixel binning, yielding images of pixel size at 0.65 $\mu\text{m}/\text{pixel}$. The image
 228 comprises 416 and 350 image tiles for WD-75684-02 and WD-75684-08, respectively, each with
 229 four channels, one of which is always Hoechst to stain DNA in the nucleus.

230

231 **Table 2.** List of protocols. As a part of the HTAN effort, all protocols and methods are deposited on
 232 Protocols.io.

Category	Center	Protocols.io link
Protocol (Biospecimen)	CHTN	Tissue Procurement and Fixation in 10% NBF https://www.protocols.io/view/tissue-procurement-fixation-with-10-nbf-6y4hfyw
Protocol (Characterization)	HMS	H&E wx.doi.org/10.17504/protocols.io.bsi8nchw
Protocol (Characterization)	HMS	FFPE Tissue Pre-treatment Before t-CyCIF on Leica Bond RX https://www.protocols.io/view/ffpe-tissue-pre-treatment-before-t-cycif-on-leica-bji2kkge
Protocol (Characterization)	HMS	Tissue Cyclic Immunofluorescence (t-CyCIF) https://www.protocols.io/view/tissue-cyclic-immunofluorescence-t-cycif-bjiukkew
Protocol (Characterization)	Broad	CODEX https://www.protocols.io/private/FAD1B1BA64C011EB8A990A58A9FEAC2A/
Protocol (Characterization)	OHSU	Multiplexed Immunohistochemistry (mIHC) https://www.protocols.io/view/mihc-staining-ohsu-coussens-lab-sop-tnp-sardana-bcdpis5n

233

234 CODEX staining and imaging

235 Coverslips were prepared following the FFPE tissue staining protocols in the Akoya Biosciences
 236 CODEX User Manual (Sections 5.4 – 5.6). Briefly, 5 μm FFPE tissue sections were cut onto PLL-

237 coated coverslips and baked for 20-25 minutes at 55 °C. Sections were cooled briefly before
238 deparaffinization and were washed for 5 minutes each as follows: twice in xylene, twice in 100%
239 ethanol, once in 90%, 70%, 50%, and 30% ethanol, and twice in deionized water. Sections were
240 moved to 1x Citrate Buffer (Vector Laboratories, H-3300) and antigen retrieval was performed in a
241 Tinto Retriever Pressure Cooker (BioSB, BSB 7008) at high pressure for 20 minutes. Sections were
242 briefly washed in deionized water before being left to incubate in deionized water at room
243 temperature for 10 minutes. Sections were briefly washed twice in Hydration Buffer (Akoya), then
244 were left to incubate in Staining Buffer (Akoya) at room temperature for 20-30 minutes. 200
245 µL/section of Antibody Cocktail was prepared according to manufacturer instructions. Sections were
246 covered with the 200 µL Antibody Cocktail and left to incubate at room temperature for 3 hours in a
247 humidity chamber. Sections were washed twice in Staining Buffer for 2 minutes, and then fixed with
248 a mixture of 1.6% PFA in Storage Buffer (Akoya) for 10 minutes. Sections were briefly washed
249 three times in 1x PBS, and then washed in ice-cold methanol for 5 minutes before being washed
250 again three times in 1x PBS. Sections were stained with 190 µL of a mixture of 20 µL Fixative
251 Reagent (Akoya) and 1 mL 1x PBS, after which they were left to incubate at room temperature for
252 20 minutes. Sections were briefly washed three times in 1X PBS and were stored in Storage Buffer
253 at 4 °C until the assay was ready to be run.

254

255 Running the CODEX Assay

256 A 96-well plate of reporter stains with Nuclear Stain (Akoya) was prepared according to Akoya
257 Biosciences CODEX User Manual (Sections 7.1 – 7.2). Stained Tissue sections were loaded onto the
258 CODEX Stage Insert (Akoya) and the Reporter Plate was loaded into the CODEX Machine. The on-
259 screen prompts were followed and the section was manually stained with a 1:2000 Nuclear Stain in
260 1x CODEX Buffer (Akoya) for 5 minutes before proceeding with following the on-screen prompts.
261 Imaging was performed on a Zeiss Axio Observer with Colibri 7 light source. Emission filters were
262 BP 450/40, BP 550/100, BP 525/50, BP 630/75, BP 647/70, BP 690/50, and TBP 425/29 + 514/31 +
263 632/100 and dichroic mirrors were QBS 405 + 492 + 575 + 653, TFT 450 + 520 + 605, TFT 395 +
264 495 + 610, and TBS 405 + 493 + 575, all from Zeiss. Overview scans were performed at 10x
265 magnification, after which 5 x 5 field of view regions were acquired using a Plan-Apochromat
266 20x/0.8 M27 Air objective (Zeiss, 420650-9902-000). 20x magnification images were acquired with
267 a 212 x 212 nm pixel size using software autofocus repeated every tile before acquiring a 17 plane z-
268 stack with 0.49 µm spacing. Tiles were stitched using a 10% overlap.

269

270

271 mIHC staining and imaging

272 The multiplex immunohistochemistry (mIHC) platform described herein involves wet and dry-lab
273 techniques that have been robustly developed to interrogate the tumor immune microenvironment in
274 situ. mIHC involves a cyclic staining process optimized for FFPE tissues with panels of antibodies
275 (12-29 per panel) designed to interrogate both lymphoid and myeloid compartments of the immune
276 system as well as cellular functional states, as previously described^{28,29}.

277
278 Pipeline implementation

279 MCMICRO was implemented in Nextflow, which was chosen for its natural integration with
280 container technologies such as Docker and Singularity, its automatic provenance tracking and
281 parallelization of image processing tasks, and its ability to specify module dependencies that may
282 change at runtime¹⁵.

283
284 Illumination correction

285 BaSiC is a Fiji / ImageJ plugin for background and shading correction, producing high accuracy
286 while requiring only a few input images¹⁹. We containerized the tool, allowing it to be executed
287 without an explicit installation of ImageJ.

288
289 Image stitching and registration using Ashlar

290 Cycle-based highly multiplexed microscopy produces multi-channel images of fixed cells using a
291 standard four/five-color microscope. Registration of the images across successive cycles is made
292 straightforward by the addition of a nuclear counterstain in every cycle. Given a set of slightly
293 overlapping images covering a tissue, we correct for mechanical stage positioning error intrinsic to
294 all microscopes using Ashlar (Alignment by Simultaneous Harmonization of Layer/Adjacency
295 Registration), a Python package for efficient mosaicing and registration of highly multiplexed
296 imagery³⁰. The overall strategy of Ashlar is as follows: (i) align tile images from the first cycle edge-
297 to-edge with their nearest neighbors (mosaicing) using phase correlation on the nuclear marker
298 channel; (ii) for the second and subsequent cycles, align each tile to the greatest overlapping tile
299 from the first cycle (registration), using phase correlation on the nuclear marker channel, and retain
300 the corrected stage coordinates, rather than the actual merged images; (iii) use the corrected
301 coordinates to assemble a single image covering the entire imaged area, including all channels from
302 all cycles. This approach minimizes the compounding of alignment errors across tiles and cycles as
303 well as temporary storage requirements for intermediate results.

304

305 Coreograph

306 Coreograph's function is to split, or 'dearray', a stitched TMA image into separate image stacks per
307 core. It employs a semantic segmentation preprocessing step to assist with identifying cores that are
308 dimmed or fragmented, which is a common issue. We trained a deep, fully connected network on
309 two classes – core tissue and background – using the popular UNet²⁴ architecture for semantic
310 segmentation. Training data consisted of cores that were well-separated, as well as cores that were
311 merged and/or fragmented, which allowed for handling situations where sample integrity was highly
312 heterogeneous. Once cores had been accentuated in the form of probability maps, they were cropped
313 from the stitched image based on their median diameter and saved as a TIFF stack. In situations
314 where the cores were too clumped, the median diameter was used to set the size of a Laplacian of
315 Gaussian (LoG) kernel in order to identify local maxima from the probability maps.

316 317 UnMicst (U-Net model for identifying cells and segmenting tissue)

318 UnMicst is a preprocessing module in MCMICRO that aids in improving downstream segmentation
319 accuracy by generating per-class probability maps to classify each pixel with a certain amount of
320 confidence. Analogous to Coreograph, it employs a UNet architecture (see above). Previously, a
321 similar UNet model was trained for nuclei segmentation to recognize two classes in Hoechst 33342 -
322 stained tonsil tissue (nuclei contours and background). Here, we train a 3-class model to extract
323 nuclei centers, nuclei contours, and background from manually annotated lung, tonsil, prostate and
324 other tissues in order to ascribe a variety of nuclei shapes. Realistic augmentations, in addition to
325 conventional on-the-fly transformations, were included by deliberately defocusing the image and
326 increasing the exposure time of the camera to simulate focus and contrast augmentations,
327 respectively. Training was performed using a batch size of 24 with the Adam Optimizer and a
328 learning rate of 0.00003 until the accuracy converged. Segmentation accuracy was estimated by
329 counting the fraction of cells in a held out test set that passed a sweeping Intersection of Union
330 (IOU) threshold.

331 332 Ilastik tissue segmentation

333 Similar to UnMicst, Ilastik assigns each pixel a probability of belonging to predetermined classes
334 (e.g., cell nucleus, membrane, background). MCMICRO relies on Ilastik's pixel classification
335 module for training and subsequent batch-processing using a random forest classifier. Ilastik
336 classifier training in MCMICRO is completed in several steps. First, regions of interest (ROIs) with a
337 user-defined width and height are randomly cropped from the WSI. Second, the ROIs are manually
338 annotated by the user on a local machine via Ilastik's graphical user interface (GUI). Third, to ensure

339 tissue portions are accurately represented in cropped images, Otsu's method is used to identify a
340 global threshold across the WSI for a particular channel of interest (e.g., nuclear staining). Finally,
341 the user exports the cropped sections that contain the desired proportion of pixels above the
342 previously determined threshold. Upon completion of the random forest training, whole slide
343 classifier predictions are deployed in headless mode (no GUI) for batch processing of large data sets
344 within MCMICRO.

345

346 Watershed segmentation via S3segmenter

347 We implemented S3segmenter, a custom marker-controlled watershed algorithm to identify nuclei
348 from the probability maps generated by UnMicst and Ilastik. Watershed markers are obtained by
349 convolving a LoG kernel, followed by a local maxima search across the image to identify seed
350 points. The size of the LoG kernel and local maxima compression are tunable parameters dependent
351 on the expected nuclei diameters in the image. As a byproduct, this method identifies false positive
352 segments in the image background. These false positives were excluded by comparing their
353 intensities to an Otsu-derived threshold calculated either on the raw image or on the probability map.
354 S3segmenter currently offers three alternative methods for cytoplasm segmentation. First, traditional
355 nonoverlapping rings (annuli) with user-defined radius are used around each nucleus. Second, a
356 Euclidean distance transform is computed around each nucleus and masked with a user-specified
357 channel, reflecting the overall shape of the whole tissue sample. An autofluorescence channel can be
358 chosen if the signal-to-image background ratio is sufficiently high. Third, the cytoplasm is
359 segmented using a marker-controlled watershed on the grayscale-weighted distance transform, where
360 the segmented nuclei are markers and the grayscale-weighted distance transform is approximated by
361 adding scaled versions of the distance transform and raw image together. This method is
362 conceptually similar to that found in the CellProfiler Identify Secondary Objects module²⁵.
363 S3segmenter is also capable of detecting puncta by convolving a small LoG kernel across the image
364 and identifying local maxima. Once nuclei and cytoplasm segmentation are complete, labelled masks
365 for each region are exported as 32-bit tiff images. Two channel tiff stacks consisting of the mask
366 outlines and raw image are also saved so that segmentation accuracy can be easily visually assessed.

367

368 MCQuant

369 Semantic segmentation in MCMICRO produces 32-bit masks, which are used to quantify pixel
370 intensity (i.e., protein expression) on multiplexed WSI for cytoplasm and nuclei. Quantification in
371 MCMICRO is carried out using scikit-image, a popular Python-based image analysis library, and
372 values of cellular spatial features are calculated for unique cells (cytoplasm and nuclei), in addition

373 to their mean pixel intensity (protein expression). The resulting spatial feature tables are exported as
374 CSV files for subsequent data analysis analogous to histoCAT¹⁷, which is implemented in
375 MATLAB.

376

377 Data availability statement

378 All software and code that produced the findings of the study, including all main and supplemental
379 figures, are available at <https://github.com/labsyspharm/mcmicro>.

380 All EMIT images are available at <https://synapse.org/EMIT> and all exemplar and tonsil images are
381 available at https://synapse.org/MCMICRO_images.

382

383 **ACKNOWLEDGEMENTS**

384 This work was funded by NIH grants U54-CA225088 and U2C-CA233262 to P.K.S. and S.S and by
385 the Ludwig Cancer Center at Harvard. D.S. was funded by an Early Postdoc Mobility fellowship (no.
386 P2ZHP3_181475) from the Swiss National Science Foundation and is a Damon Runyon Fellow
387 supported by the Damon Runyon Cancer Research Foundation (DRQ-03-20). Z.M. is supported by
388 NCI grant R50-CA252138. We thank Dana-Farber/Harvard Cancer Center in Boston, MA, for the
389 use of the Specialized Histopathology Core, which provided TMA construction and sectioning
390 services. Dana-Farber/Harvard Cancer Center is supported in part by an NCI Cancer Center Support
391 Grant P30 CA06516. Tissue samples were provided by the NCI Cooperative Human Tissue Network
392 (CHTN).

393 **OUTSIDE INTERESTS**

394 PKS is a member of the SAB or BOD member of Applied Biomath, RareCyte Inc., and Glencoe
395 Software, which distributes a commercial version of the OMERO database; PKS is also a member of
396 the NanoString SAB. In the last five years the Sorger lab has received research funding from
397 Novartis and Merck. Sorger declares that none of these relationships have influenced the content of
398 this manuscript. SS is a consultant for RareCyte Inc. A. R. is a cofounder and equity holder of
399 Celsius Therapeutics, an equity holder in Immunitas and, until 31 July 2020, was an SAB member of
400 Thermo Fisher Scientific, Syros Pharmaceuticals, Neogene Therapeutics and Asimov. Since August
401 1, 2020, A. R. has been an employee of Genentech. The other authors declare no outside interests.

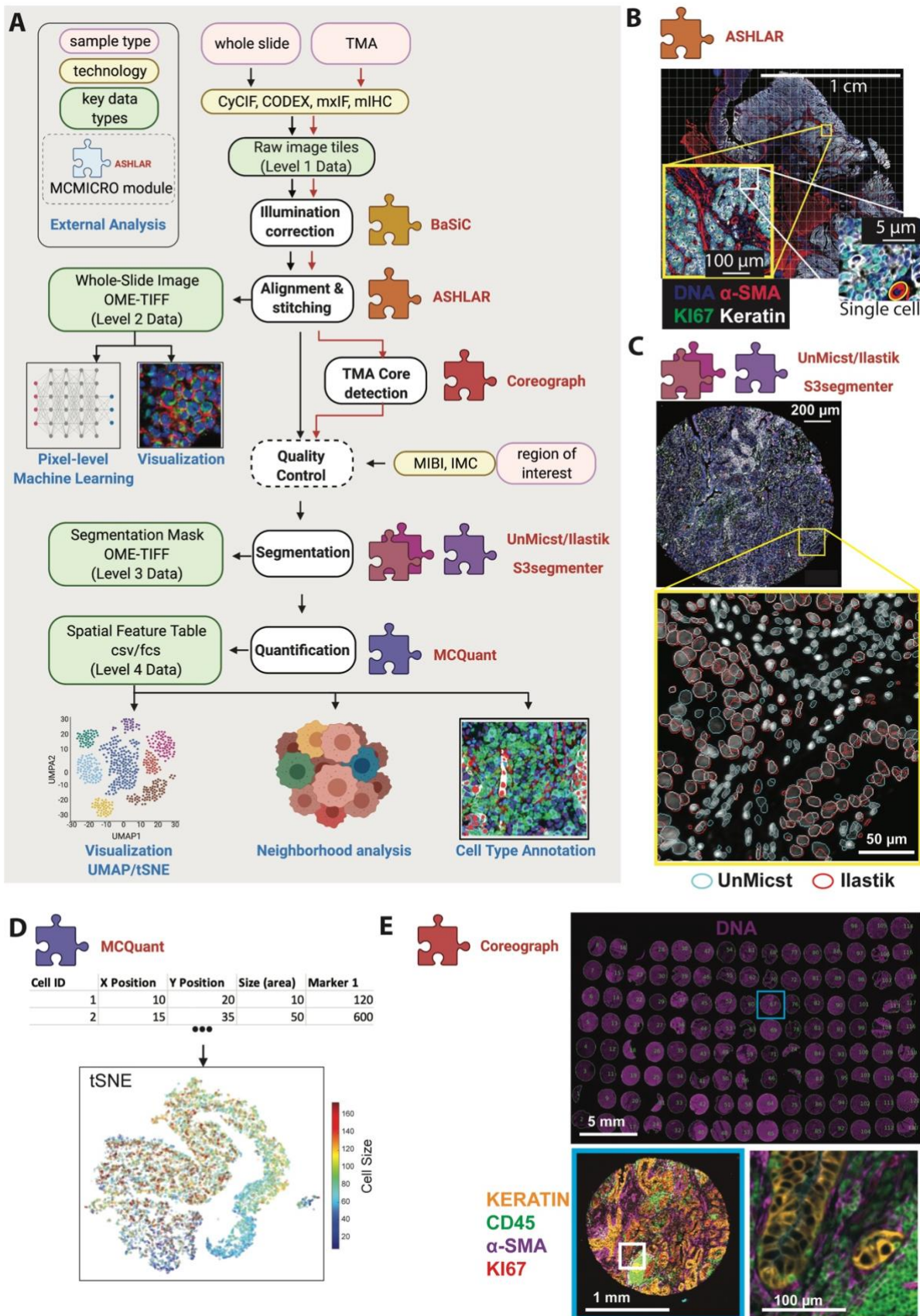
402 **REFERENCES**

- 403 1. Keren, L. *et al.* A Structured Tumor-Immune Microenvironment in Triple Negative Breast Cancer
404 Revealed by Multiplexed Ion Beam Imaging. *Cell* **174**, 1373-1387.e19 (2018).
- 405 2. CRUK IMAXT Grand Challenge Team *et al.* Imaging mass cytometry and multiplatform
406 genomics define the phenogenomic landscape of breast cancer. *Nat. Cancer* **1**, 163–175 (2020).
- 407 3. Jackson, H. W. *et al.* The single-cell pathology landscape of breast cancer. *Nature* **578**, 615–620
408 (2020).
- 409 4. Schürch, C. M. *et al.* Coordinated Cellular Neighborhoods Orchestrate Antitumoral Immunity at
410 the Colorectal Cancer Invasive Front. *Cell* **182**, 1341-1359.e19 (2020).
- 411 5. Abels, E. & Pantanowitz, L. Current state of the regulatory trajectory for whole slide imaging
412 devices in the USA. *J. Pathol. Inform.* **8**, 23 (2017).
- 413 6. Evans, A. J. *et al.* US Food and Drug Administration Approval of Whole Slide Imaging for
414 Primary Diagnosis: A Key Milestone Is Reached and New Questions Are Raised. *Arch. Pathol.*
415 *Lab. Med.* **142**, 1383–1387 (2018).
- 416 7. Lin, J.-R. *et al.* Highly multiplexed immunofluorescence imaging of human tissues and tumors
417 using t-CyCIF and conventional optical microscopes. *eLife* **7**, e31657 (2018).
- 418 8. Vickovic, S. *et al.* High-definition spatial transcriptomics for in situ tissue profiling. *Nat. Methods*
419 **16**, 987–990 (2019).
- 420 9. Rodriques, S. G. *et al.* Slide-seq: A scalable technology for measuring genome-wide expression at
421 high spatial resolution. *Science* **363**, 1463–1467 (2019).
- 422 10. Chen, K. H., Boettiger, A. N., Moffitt, J. R., Wang, S. & Zhuang, X. Spatially resolved,
423 highly multiplexed RNA profiling in single cells. *Science* **348**, aaa6090–aaa6090 (2015).
- 424 11. Li, B. *et al.* Cumulus provides cloud-based data analysis for large-scale single-cell and
425 single-nucleus RNA-seq. *Nat. Methods* **17**, 793–798 (2020).

- 426 12. Merkel, D. Docker: Lightweight Linux Containers for Consistent Development and
427 Deployment. *Linux J* **2014**, (2014).
- 428 13. Common Workflow Language (CWL) Workflow Description, v1.0.2.
429 <https://www.commonwl.org/v1.0/Workflow.html>.
- 430 14. Rozenblatt-Rosen, O. *et al.* The Human Tumor Atlas Network: Charting Tumor Transitions
431 across Space and Time at Single-Cell Resolution. *Cell* **181**, 236–249 (2020).
- 432 15. Di Tommaso, P. *et al.* Nextflow enables reproducible computational workflows. *Nat.*
433 *Biotechnol.* **35**, 316–319 (2017).
- 434 16. Kurtzer, G. M., Sochat, V. & Bauer, M. W. Singularity: Scientific containers for mobility of
435 compute. *PLOS ONE* **12**, e0177459 (2017).
- 436 17. Schapiro, D. *et al.* histoCAT: analysis of cell phenotypes and interactions in multiplex image
437 cytometry data. *Nat. Methods* **14**, 873–876 (2017).
- 438 18. Saka, S. K. *et al.* Immuno-SABER enables highly multiplexed and amplified protein imaging
439 in tissues. *Nat. Biotechnol.* **37**, 1080–1090 (2019).
- 440 19. Peng, T. *et al.* A BaSiC tool for background and shading correction of optical microscopy
441 images. *Nat. Commun.* **8**, 14836 (2017).
- 442 20. Berg, S. *et al.* ilastik: interactive machine learning for (bio)image analysis. *Nat. Methods* **16**,
443 1226–1232 (2019).
- 444 21. Linkert, M. *et al.* Metadata matters: access to image data in the real world. *J. Cell Biol.* **189**,
445 777–782 (2010).
- 446 22. Iizuka, O. *et al.* Deep Learning Models for Histopathological Classification of Gastric and
447 Colonic Epithelial Tumours. *Sci. Rep.* **10**, 1504 (2020).
- 448 23. Campanella, G. *et al.* Clinical-grade computational pathology using weakly supervised deep
449 learning on whole slide images. *Nat. Med.* **25**, 1301–1309 (2019).

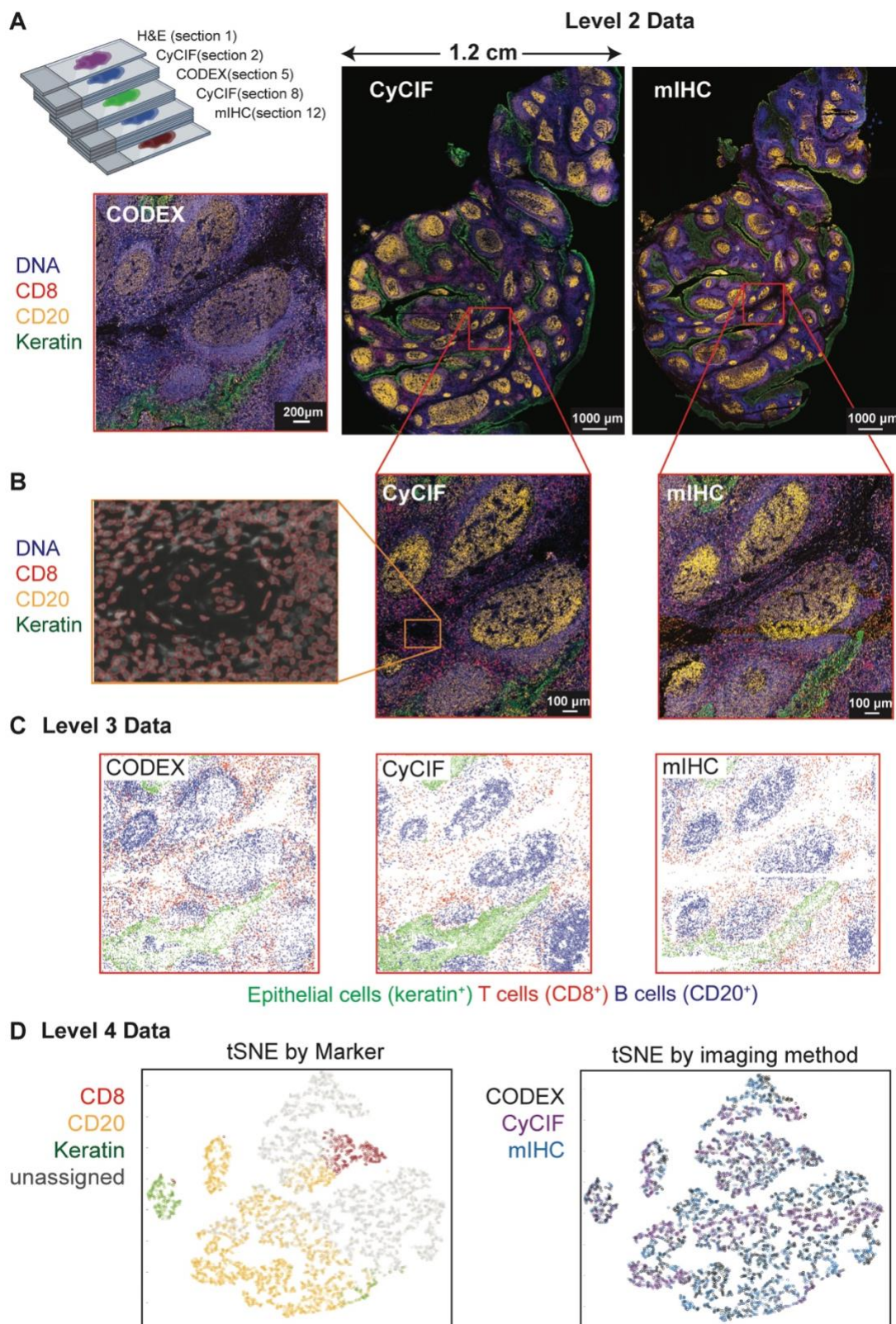
- 450 24. Ronneberger, O., Fischer, P. & Brox, T. U-Net: Convolutional Networks for Biomedical
451 Image Segmentation. in *Medical Image Computing and Computer-Assisted Intervention –*
452 *MICCAI 2015* (eds. Navab, N., Hornegger, J., Wells, W. M. & Frangi, A. F.) vol. 9351 234–241
453 (Springer International Publishing, 2015).
- 454 25. McQuin, C. *et al.* CellProfiler 3.0: Next-generation image processing for biology. *PLOS Biol.*
455 **16**, e2005970 (2018).
- 456 26. Stolovitzky, G., Prill, R. J. & Califano, A. Lessons from the DREAM2 Challenges. *Ann. N.*
457 *Y. Acad. Sci.* **1158**, 159–195 (2009).
- 458 27. Wilkinson, M. D. *et al.* The FAIR Guiding Principles for scientific data management and
459 stewardship. *Sci. Data* **3**, 160018 (2016).
- 460 28. Tsujikawa, T. *et al.* Quantitative Multiplex Immunohistochemistry Reveals Myeloid-
461 Inflamed Tumor-Immune Complexity Associated with Poor Prognosis. *Cell Rep.* **19**, 203–217
462 (2017).
- 463 29. Banik, G. *et al.* High-dimensional multiplexed immunohistochemical characterization of
464 immune contexture in human cancers. *Methods Enzymol.* **635**, 1–20 (2020).
- 465 30. *ASHLAR*.
466 <https://github.com/labsyspharm/ashlar>.
467

468 **FIGURE 1**



470 **Fig. 1: MCMICRO pipeline overview. Modules highlighted in bold red are developed and/or**
471 **containerized in-house. (A)** A schematic representation of a canonical workflow for end-to-end
472 image processing of multiplexed whole-slide and TMA using MCMICRO. Shown is a flow of inputs
473 (pink rectangles) from imaging technologies (yellow rectangles) through image processing steps
474 (white rectangles) that are implemented in software modules (puzzle pieces) to produce key data
475 types (green rectangles). Data flows associated with the whole slide and TMA are represented with
476 black and red arrows, respectively. Quality control is highlighted with a dashed border. **(B-E)**
477 Highlights of individual software modules incorporated into MCMICRO. **B** ASHLAR is used to
478 stitch and register individual CyCIF image tiles with subcellular accuracy (yellow zoom-in). This
479 panel depicts a 484 tile (22 x 22) t-CyCIF, whole-slide, mosaic image of a human colorectal cancer
480 in four channels: Hoechst 33342-stained nuclear DNA (blue), α -smooth muscle actin (α -SMA; red),
481 the Ki-67 proliferation marker (green) and cytokeratin (white). An interactive on-line visualization of
482 these data can be found at: <https://www.cycif.org/data/tnp-2020/osd-crc-case-1-ffpe-cycif-stack>. **C**
483 Two different segmentation masks computed by UnMicst (blue) and Ilastik (red) overlaid on an
484 image of nuclei from an EMIT TMA core. **D** A schematic of the first rows and columns of a Spatial
485 Feature Table used for visualization using tSNE. **E** A CyCIF image of an EMIT TMA de-arrayed
486 using Coreograph to identify individual cores, which are subsequential extracted and analyzed in
487 high-resolution. Below, a five-color image of a single lung adenocarcinoma core is shown for
488 channels corresponding to Hoechst 33342-stained DNA (white), cytokeratin (orange), the immune-
489 cell marker CD45 (green), α -SMA (magenta) and Ki-67 (red)).
490

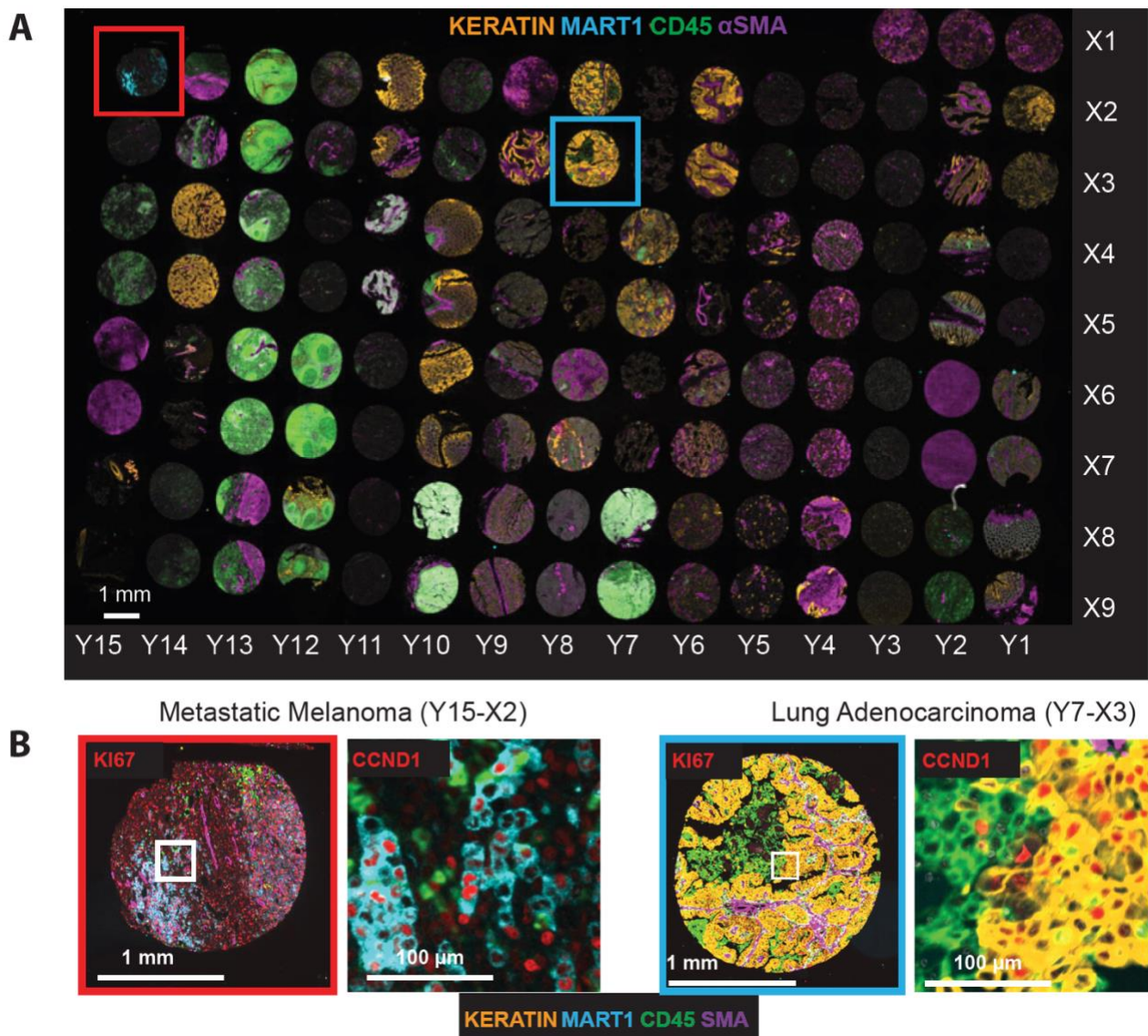
491 **FIGURE 2:**



493 **Fig. 2: Comparison of images of human tonsil collected using three different technologies and**
494 **processed using MCMICRO. A.** Serial sections of a single tissue block imaged using H&E, 11-
495 marker CODEX, 27-marker CyCIF, and 16-marker mIHC. The sectioning plan shows the position of
496 each 5 µm section within the block: H&E section 1, CyCIF section 2, CODEX section 5 and mIHC
497 section 12. Images show selected channels as follows: Hoechst 33342 (blue), CD20 (orange),
498 Keratin (green), and CD8 (red). The CODEX image shows only a specific region (red border) of the
499 specimen visible in whole-slide images to the right. **B.** Higher magnification images of the data
500 above highlighting individual cells and segmentation masks generated with UnMicst. **C.** Centroids of
501 the single cell mask for CODEX, CyCIF and mIHC are colored by marker expression to identify cell
502 types. Epithelial cells of the tonsil mucosa stain positive for pan-cytokeratin (green), cytotoxic T
503 cells stain positive for CD8 (red); and B cells stain positive for CD20 (blue). **D.** t-SNE of combined
504 CODEX, CyCIF and mIHC data demonstrating clustering by marker expression (left) but not
505 imaging technology (right).
506

507 **FIGURE S1**

Figure S1



508

509 **Figure S1. The EMIT dataset spanning 123 tissue cores across 34 cancer, non-neoplastic**

510 **diseases, and normal tissue type. A.** CyCIF whole slide image of EMIT visualizing Hoechst

511 33342-stained nuclear DNA (white), Keratin (orange), MART1 (cyan), CD45 (green) and SMA

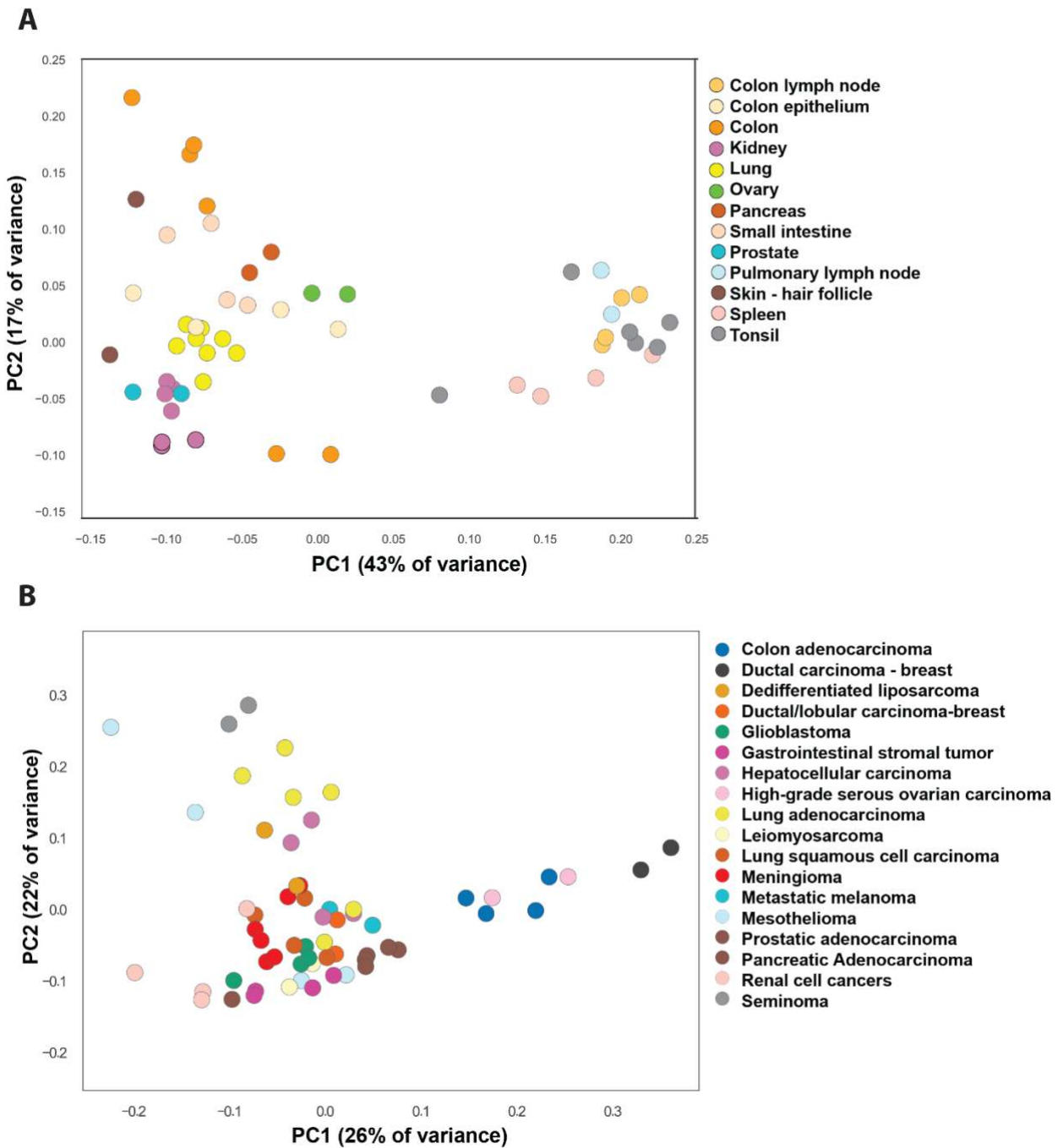
512 (purple). **B.** A zoom-in view of a metastatic melanoma (left, red box) and a lung adenocarcinoma

513 (right, blue box) core. The highest zoom level is highlighted with white boxes in the corresponding

514 low magnification images.

515

Figure S2

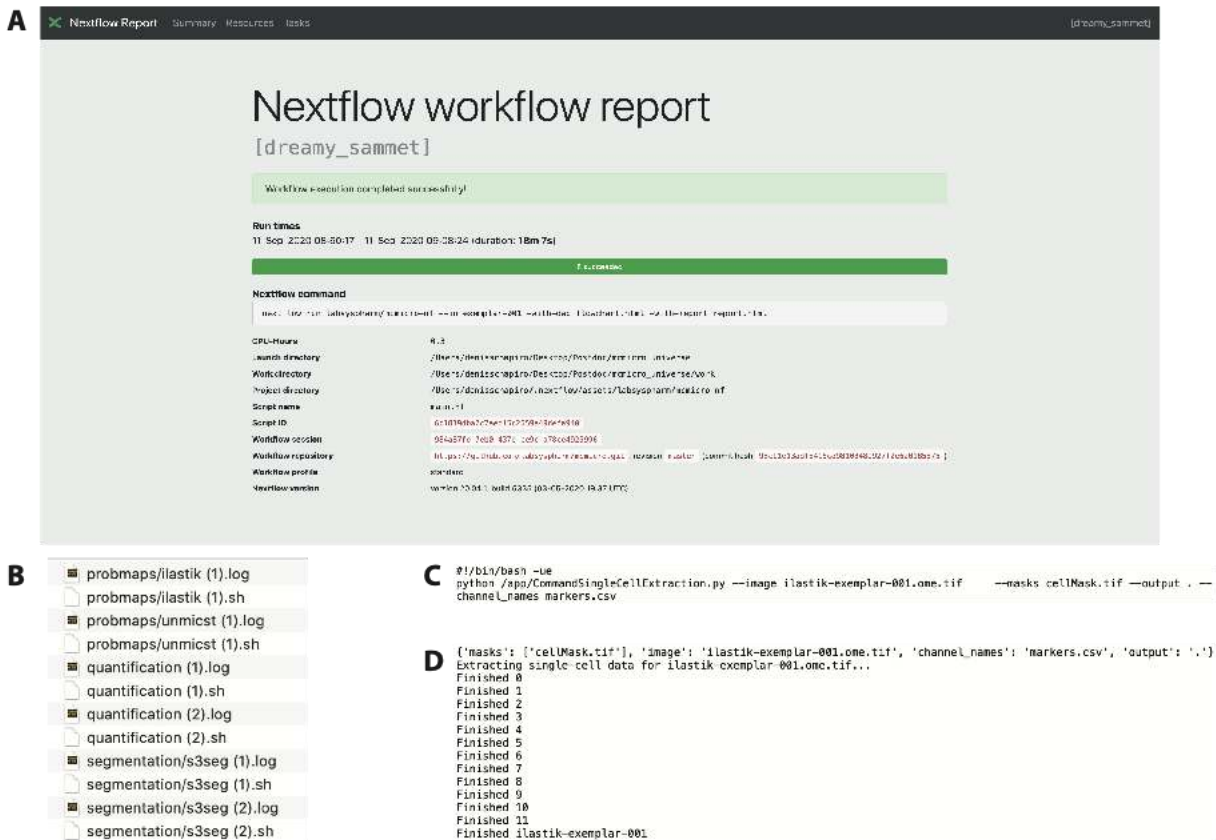


516

517 **Figure S2. Principal component analysis (PCA) of Spatial Feature Tables derived from EMIT**
518 **images. A.** represents normal tissues and **B.** cancer tissues. Independent cores cluster to a substantial
519 degree by tissue or cancer type; some variation is expected because tumors had different grades and
520 derive from different individuals. Data from the following antibodies was used to generate the data:
521 CD73, MART1, KI67, pan-cytokeratin, CD45, ECAD, α -SMA, CD32, CDKN1A, CCNA2,
522 CDKN1C, CDKN1B, CCND1, cPARP, CCNB1, PCNA and CDK2.

523

524 **FIGURE S3**

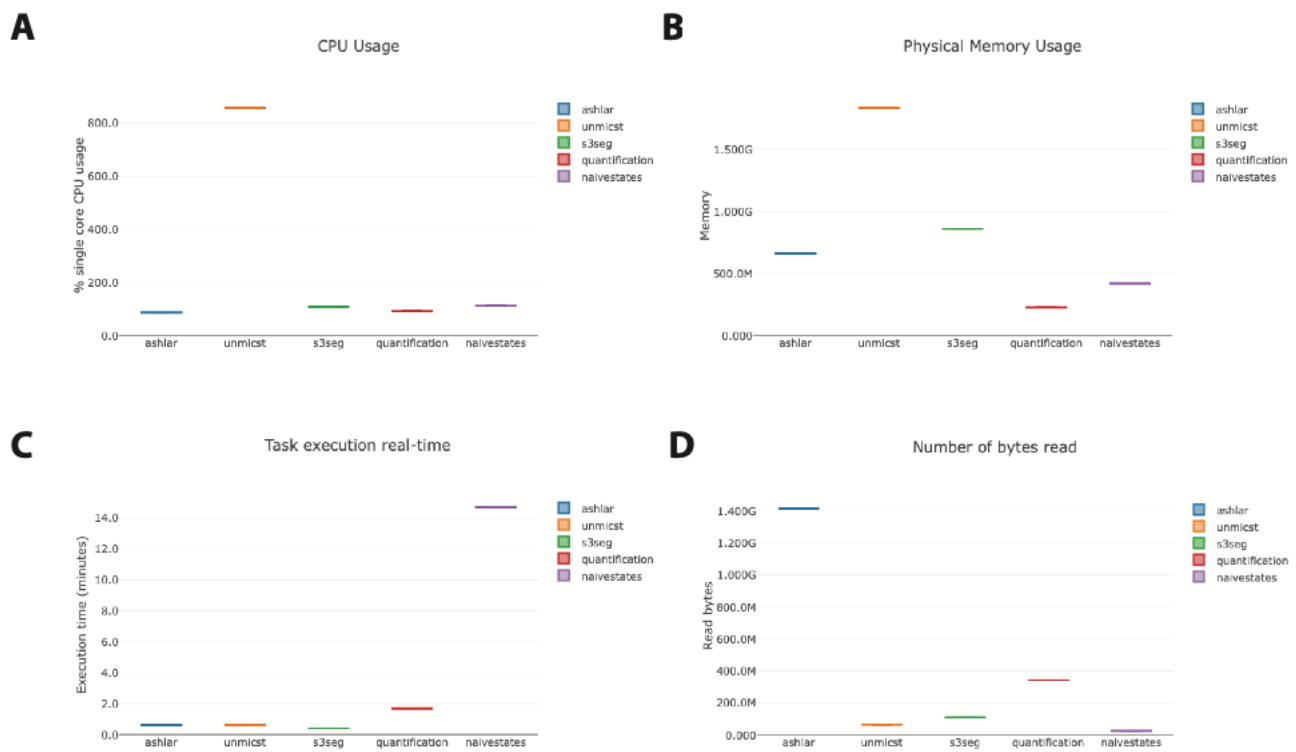


525

526 **Figure S3. Nextflow enables reproducible data processing using the provenance module. A.**
527 Nextflow report provides detailed documentation for used resources, directories, repositories
528 (including commit hash) and the corresponding execution times. The report is browser based and
529 interactive. **B-D.** Provenance reconstruction enabled by recording each executed command (.sh) and
530 its output (.log). Representative examples of a command and its output are shown in (C) and (D),
531 respectively.

532

533 **FIGURE S4**



534

535

536 **Figure S4. Detailed insight into the computational resources required by each module,**

537 **generated by Nextflow.** The data is viewed as an interactive browser-based report. **A.** CPU usage is

538 recorded as either % single core CPU usage (visualized) or % CPUs allocated. **B.** Physical memory

539 usage is recorded as either RAM only (visualized), RAM + Disk swap or % RAM allocated. **C.** Job

540 duration is recorded as either execution time (visualized) or % time allocated. **D.** Input/Output (I/O)

541 records both read (visualized) and written bytes.

542

543 **Table S1: Highly multiplexed imaging methods**

Non-cyclic metal-based	Cyclic fluorescence imaging		Cyclic immune-histochemistry
	cyclic-stained	single-stained	
Imaging Mass Cytometry (IMC) ¹	CODEX ²	MxIF ³	mIHC ⁴
Multiplexed Ion Beam Imaging (MIBI) ⁵	Immuno-SABER ⁶	CyCIF ⁷	MICSSS ⁸
		4i ⁹	

544

545 **Table S1:** Orange labeled methods were successfully processed by MCMICRO on publicly available
546 datasets. Green labeled methods are additionally tested on images unique to this study with detailed
547 description in the documentation.

548

549 **Table S2: Available open-source tools for image processing, analysis and visualization**

550

Software	Scalable	Whole slide processing	Stitching and registration	Modular	Segmentation	Analysis	GUI
MCMICRO	Yes	Yes	Yes	Yes	Yes	Yes	No
Cytokit ¹⁰	Yes	No (tiles)	No	No	Yes	Yes	Yes
starfish ¹¹	Yes	No (tiles)	No	Yes	Yes	Yes	No
histoCAT ¹²	No	Yes	No	Yes	No	Yes	Yes
QuPath ¹³	No	Yes	No	No	Yes	Yes	Yes
CytoMAP ¹⁴	No	Yes	No	No	No	Yes	Yes
Facetto ¹⁵	No	Yes	No	No	No	Yes	Yes
napari ¹⁶	Visualization tool						
OMERO ¹⁷	Visualization tool						
Minerva ¹⁸	Visualization tool						

551

552 **Table S2: List of open-source tools available for highly multiplexed image processing.**

553

554 **Supplementary table references:**

- 555 1. Giesen, C., Wang, H. A. O., Schapiro, D., Zivanovic, N., Jacobs, A., Hattendorf, B., Schüffler, P. J., Grolimund, D., Buhmann, J. M., Brandt, S.,
556 Varga, Z., Wild, P. J., Günther, D. & Bodenmiller, B. Highly multiplexed imaging of tumor tissues with subcellular resolution by mass cytometry.
557 *Nat Methods* **11**, 417–422 (2014).
- 558 2. Goltsev, Y., Samusik, N., Kennedy-Darling, J., Bhate, S., Hale, M., Vazquez, G., Black, S. & Nolan, G. P. Deep Profiling of Mouse Splenic
559 Architecture with CODEX Multiplexed Imaging. *Cell* **174**, 968–981.e15 (2018).
- 560 3. Gerdes, M. J., Sevinsky, C. J., Sood, A., Adak, S., Bello, M. O., Bordwell, A., Can, A., Corwin, A., Dinn, S., Filkins, R. J., Hollman, D., Kamath,
561 V., Kaanumalle, S., Kenny, K., Larsen, M., Lazare, M., Li, Q., Lowes, C., McCulloch, C. C., McDonough, E., Montalto, M. C., Pang, Z., Rittscher,
562 J., Santamaria-Pang, A., Sarachan, B. D., Seel, M. L., Seppo, A., Shaikh, K., Sui, Y., Zhang, J. & Ginty, F. Highly multiplexed single-cell analysis
563 of formalin-fixed, paraffin-embedded cancer tissue. *PNAS* **110**, 11982–11987 (2013).
- 564 4. Tsujikawa, T., Kumar, S., Borkar, R. N., Azimi, V., Thibault, G., Chang, Y. H., Balter, A., Kawashima, R., Choe, G., Sauer, D., El Rassi, E.,
565 Clayburgh, D. R., Kulesz-Martin, M. F., Lutz, E. R., Zheng, L., Jaffee, E. M., Leyshock, P., Margolin, A. A., Mori, M., Gray, J. W., Flint, P. W. &
566 Coussens, L. M. Quantitative Multiplex Immunohistochemistry Reveals Myeloid-Inflamed Tumor-Immune Complexity Associated with Poor
567 Prognosis. *Cell Reports* **19**, 203–217 (2017).
- 568 5. Angelo, M., Bendall, S. C., Finck, R., Hale, M. B., Hitzman, C., Borowsky, A. D., Levenson, R. M., Lowe, J. B., Liu, S. D., Zhao, S., Natkunam,
569 Y. & Nolan, G. P. Multiplexed ion beam imaging (MIBI) of human breast tumors. *Nat Med* **20**, 436–442 (2014).
- 570 6. Saka, S. K., Wang, Y., Kishi, J. Y., Zhu, A., Zeng, Y., Xie, W., Kirli, K., Yapp, C., Cicconet, M., Beliveau, B. J., Lapan, S. W., Yin, S., Lin, M.,
571 Boyden, E. S., Kaeser, P. S., Pihan, G., Church, G. M. & Yin, P. Immuno-SABER enables highly multiplexed and amplified protein imaging in
572 tissues. *Nat Biotechnol* **37**, 1080–1090 (2019).
- 573 7. Lin, J.-R., Izar, B., Wang, S., Yapp, C., Mei, S., Shah, P. M., Santagata, S. & Sorger, P. K. Highly multiplexed immunofluorescence imaging of
574 human tissues and tumors using t-CyCIF and conventional optical microscopes. *eLife* **7**, e31657 (2018).
- 575 8. Remark, R., Merghoub, T., Grabe, N., Litjens, G., Damotte, D., Wolchok, J. D., Merad, M. & Gnjatic, S. In-depth tissue profiling using
576 multiplexed immunohistochemical consecutive staining on single slide. *Science Immunology* **1**, aaf6925–aaf6925 (2016).
- 577 9. Gut, G., Herrmann, M. D. & Pelkmans, L. Multiplexed protein maps link subcellular organization to cellular states. *Science* **361**, eaar7042 (2018).
- 578 10. Czech, E., Aksoy, B. A., Aksoy, P. & Hammerbacher, J. Cytokit: a single-cell analysis toolkit for high dimensional fluorescent microscopy
579 imaging. *BMC Bioinformatics* **20**, 448 (2019).
- 580 11. <https://spacex-starfish.readthedocs.io/en/latest/>.
- 581 12. Schapiro, D., Jackson, H. W., Raghuraman, S., Fischer, J. R., Zanotelli, V. R. T., Schulz, D., Giesen, C., Catena, R., Varga, Z. & Bodenmiller, B.
582 histoCAT: analysis of cell phenotypes and interactions in multiplex image cytometry data. *Nat Methods* **14**, 873–876 (2017).
- 583 13. Bankhead, P., Loughrey, M. B., Fernández, J. A., Dombrowski, Y., McArt, D. G., Dunne, P. D., McQuaid, S., Gray, R. T., Murray, L. J., Coleman,
584 H. G., James, J. A., Salto-Tellez, M. & Hamilton, P. W. QuPath: Open source software for digital pathology image analysis. *Sci Rep* **7**, 16878
585 (2017).
- 586 14. Stoltzfus, C. R., Filipek, J., Gern, B. H., Olin, B. E., Leal, J. M., Wu, Y., Lyons-Cohen, M. R., Huang, J. Y., Paz-Stoltzfus, C. L., Plumlee, C. R.,
587 Pöschinger, T., Urdahl, K. B., Perro, M. & Germer, M. Y. CytoMAP: A Spatial Analysis Toolbox Reveals Features of Myeloid Cell Organization in
588 Lymphoid Tissues. *Cell Reports* **31**, 107523 (2020).
- 589 15. Krueger, R., Beyer, J., Jang, W.-D., Kim, N. W., Sokolov, A., Sorger, P. K. & Pfister, H. Facetto: Combining Unsupervised and Supervised
590 Learning for Hierarchical Phenotype Analysis in Multi-Channel Image Data. *IEEE Trans. Visual. Comput. Graphics* **26**, 227–237 (2020).
- 591 16. Sofroniew, N., Talley Lambert, Evans, K., Nunez-Iglesias, J., Yamauchi, K., Solak, A. C., Buckley, G., Bokota, G., Tung, T., Ziyangzi, Freeman,
592 J., Boone, P., Winston, P., Loic Royer, Har-Gil, H., Axelrod, S., Rokem, A., Bryant, Hector, Mars Huang, Pranathi Vemuri, Dunham, R.,
593 Jakirkham, Siqueira, A. D., Bhavya Chopra, Wood, C., Gohlke, C., Bennett, D., DragaDoncila & Perlman, E. *napari/napari: 0.3.5*. (Zenodo,
594 2020). doi:10.5281/ZENODO.3555620
- 595 17. Allan, C., Burel, J.-M., Moore, J., Blackburn, C., Linkert, M., Loynton, S., Macdonald, D., Moore, W. J., Neves, C., Patterson, A., Porter, M.,
596 Tarkowska, A., Loranger, B., Avondo, J., Lagerstedt, I., Lianas, L., Leo, S., Hands, K., Hay, R. T., Patwardhan, A., Best, C., Kleywegt, G. J.,
597 Zanetti, G. & Swedlow, J. R. OMERO: flexible, model-driven data management for experimental biology. *Nat Methods* **9**, 245–253 (2012).
- 598 18. Rashid, R., Chen, Y.-A., Hoffer, J., Muhlich, J. L., Lin, J.-R., Krueger, R., Pfister, H., Mitchell, R., Santagata, S. & Sorger, P. K. *Online narrative*
599 *guides for illuminating tissue atlas data and digital pathology images*. (Scientific Communication and Education, 2020).
600 doi:10.1101/2020.03.27.001834

